

Article

Elucidating the Influence of Electric Fields toward CO₂ Activation on YSZ (111)

Nisa Ulumuddin ¹, Fanglin Che ², Jung-II Yang ³, Su Ha ¹ and Jean-Sabin McEwen ^{1,4,5,6,7,*}

¹ The Gene & Linda Voiland School of Chemical Engineering and Bioengineering, Washington State University, Pullman, WA 99164, USA; nisa.ulumuddin@wsu.edu (N.U.); suha@wsu.edu (S.H.)

² Department of Chemical Engineering, University of Massachusetts, Lowell, MA 01854, USA; Fanglin_Che@uml.edu

³ Clean Fuel Laboratory, Korea Institute of Energy Research, Daejeon 34129, Korea; yangji@kier.re.kr

⁴ Pacific Northwest National Laboratory, Institute for Integrated Catalysis, Richland, WA 99352, USA

⁵ Department of Physics and Astronomy, Washington State University, Pullman, WA 99164, USA

⁶ Department of Chemistry, Washington State University, Pullman, WA 99164, USA

⁷ Department of Biological Systems Engineering, Washington State University, Pullman, WA 99164, USA

* Correspondence: js.mcewen@wsu.edu

Abstract: Despite its high thermodynamic stability, the presence of a negative electric field is known to facilitate the activation of CO₂ through electrostatic effects. To utilize electric fields for a reverse water gas shift reaction, it is critical to elucidate the role of an electric field on a catalyst surface toward activating a CO₂ molecule. We conduct a first-principles study to gain an atomic and electronic description of adsorbed CO₂ on YSZ (111) surfaces when external electric fields of +1 V/Å, 0 V/Å, and −1 V/Å are applied. We find that the application of an external electric field generally destabilizes oxide bonds, where the direction of the field affects the location of the most favorable oxygen vacancy. The direction of the field also drastically impacts how CO₂ adsorbs on the surface. CO₂ is bound by physisorption when a +1 V/Å field is applied, a similar interaction as to how it is adsorbed in the absence of a field. This interaction changes to chemisorption when the surface is exposed to a −1 V/Å field value, resulting in the formation of a CO₃[−] complex. The strong interaction is reflected through a direct charge transfer and an orbital splitting within the O_{lattice} *p*-states. While CO₂ remains physisorbed when a +1 V/Å field value is applied, our total density of states analysis indicates that a positive field pulls the charge away from the adsorbate, resulting in a shift of its bonding and antibonding peaks to higher energies, allowing a stronger interaction with YSZ (111). Ultimately, the effect of an electric field toward CO₂ adsorption is not negligible, and there is potential in utilizing electric fields to favor the thermodynamics of CO₂ reduction on heterogeneous catalysts.

Keywords: CO₂ reduction; electric field; catalysis; density functional theory; yttria stabilized zirconia



Citation: Ulumuddin, N.; Che, F.; Yang, J.-I.; Ha, S.; McEwen, J.-S. Elucidating the Influence of Electric Fields toward CO₂ Activation on YSZ (111). *Catalysts* **2021**, *11*, 271. <https://doi.org/10.3390/catal11020271>

Academic Editors: Roger Rousseau, Vassiliki-Alexandra Glezakou, Jamie Holladay, Kelsey Stoerzinger, Olivier Gutierrez and Juan Lopez-Ruiz

Received: 27 January 2021

Accepted: 11 February 2021

Published: 18 February 2021

Publisher's Note: MDPI stays neutral with regard to jurisdictional claims in published maps and institutional affiliations.



Copyright: © 2021 by the authors. Licensee MDPI, Basel, Switzerland. This article is an open access article distributed under the terms and conditions of the Creative Commons Attribution (CC BY) license (<https://creativecommons.org/licenses/by/4.0/>).

1. Introduction

Global energy demand has rapidly increased over the past decades due to the increase in world population and rapid economic development of developing countries [1,2]. It is expected that this increasing trend in the world energy demand will continue in the foreseeable future. In order to meet this energy demand, the consumption of fossil fuels has dramatically increased and is predicted to continuously increase as well [3]. Because fossil fuels produce large quantities of CO₂ when burned, their large consumption has negatively impacted our environments (e.g., global warming due to CO₂ accumulation in the atmosphere) [4,5]. Among various alternative and renewable energy technologies, hydrogen-based technologies are considered as one of the most promising strategies to replace conventional fossil fuel-based energy technologies because it only produces H₂O byproducts when it combusts [6,7]. However, the majority of hydrogen is currently

produced via steam methane reforming (SMR). Thus, current hydrogen production is still bounded to non-renewable sources and generates a large amount of CO₂ emissions (e.g., ~380–420 kg_{CO₂}/Nm³_{H₂}) [8].

Biogas is considered a viable renewable source to produce hydrogen, as described in Figure 1. To produce green hydrogen from biogas at an economically feasible price (e.g., DOE target of US \$4/kg of H₂), the raw biogas needs to be reformed without the CO₂ gas separation step. One of the technical challenges with reforming the raw biogas is its high tendency for coke formation, which eventually deactivates the catalyst [9]. In order to mitigate this coking issue, one can increase the steam-to-carbon (S/C) ratio for the raw biogas reforming process [8,9]. However, this high (S/C) operation increases the overall operating energy consumption requirement and cost to produce the hydrogen gas. Thus, it is highly desired to find new reforming technologies that can process raw biogas without using a large amount of steam and at a lower operating reaction temperature.

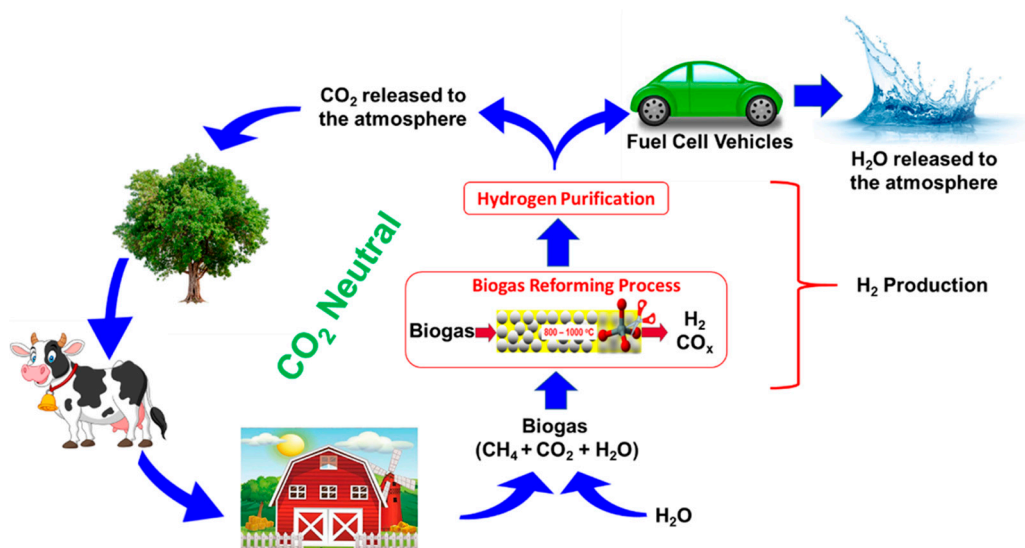


Figure 1. Schematic of biogas energy cycle.

Recently, electric-field-assisted fuel reforming has been investigated in an attempt to prevent coking and to reduce the reaction temperature for the conventional steam methane reforming reaction [10–12]. By applying an external electric field, it is possible to manipulate both the thermodynamic (e.g., equilibrium constant) and kinetic (e.g., molecular orientation and electronic interaction between the reactive species and the catalyst) aspects of the steam methane reforming reaction [11]. For example, when a positive electric field is applied to the Ni catalyst surface during the steam methane reforming reaction, one can increase the adsorption rate of water molecules over the catalyst surface by aligning its dipole moment with the orientation of the external electric field that is applied [10,13]. As the local concentration of water molecules at the catalyst surface increases with the electric field strength, the formation of coke can be significantly mitigated even at the low S/C ratio of 2 [10]. Furthermore, methane conversion increases when the positive electric field is applied over the Ni catalytic surface by affecting the energetics of its key intermediates to influence its reaction pathways [11,12].

In addition to influencing the CH₄ and H₂O chemistries during the raw biogas steam reforming process under the surface electric field condition, one also needs to efficiently convert CO₂ into CO so that they can be further converted to valuable chemicals and fuels. Various pathways exist for the reduction of CO₂ to CO. The redox-mechanism, where the reduction of CO₂ and oxidation of the catalyst occurs simultaneously, has been proposed for various catalysts [14,15]. Other well-known pathways are categorized as the association mechanism, where CO₂ adsorbs on the catalyst and reacts with protons to form

intermediate species such as formate, carboxyl, carbonate, and bicarbonate [16,17]. Either routes can occur on reducible oxides [18–20]. Regardless of the mechanism, however, the activation of CO₂ is consistently an energetically costly step, as it requires the transfer of an electron to the CO₂ adsorbate, forming a radical anion [21].

Recent work by Xiao et al. [22] has shown how the oxidation state of Cu influences the adsorption strength of CO. Furthermore, since water has a permanent dipole moment that either aligns or anti-aligns with the electric field vector (resulting in an increased or decreased adsorption strength, respectively) [13], we co-adsorbed water in the vicinity of a CO₂ molecule to see if one can find a similar enhancement effect of the electric field with regard to the adsorption of CO₂. This would facilitate its dissociative adsorption into CO and O adspecies as suggested by Xiao et al. [22]. Unfortunately, our preliminary work shown in Figure 2 demonstrates that electric field effects were negligible toward CO₂ adsorption on Ni (111), as its adsorption energy remained weak between -0.16 eV and -0.04 eV. The adsorption of CO₂ is typically enhanced in the presence of active O, which can be provided by oxide-supported catalysts [16,20,23]. However, despite the high selectivity (90–99%) for CO₂ reduction, most conversion rates for the reversed water gas shift reaction are limited to below 20% over oxide-supported catalysts [16]. The potential for enhancing CO₂ activation using electric fields has been explored by Oshima et al. [24]. Further, recent field emission studies by Lambeets et al., where a high electric field is applied at the apex of a field Rh emitter tip, have also shown evidence of CO₂ activation [25]. This shows that even though CO₂ is a very stable molecule with no permanent dipole moment, it can be polarized under the applied electric field [26]. However, a theoretical study specifically investigating changes upon the catalyst's electronic structure induced by the electric field has not been done yet.

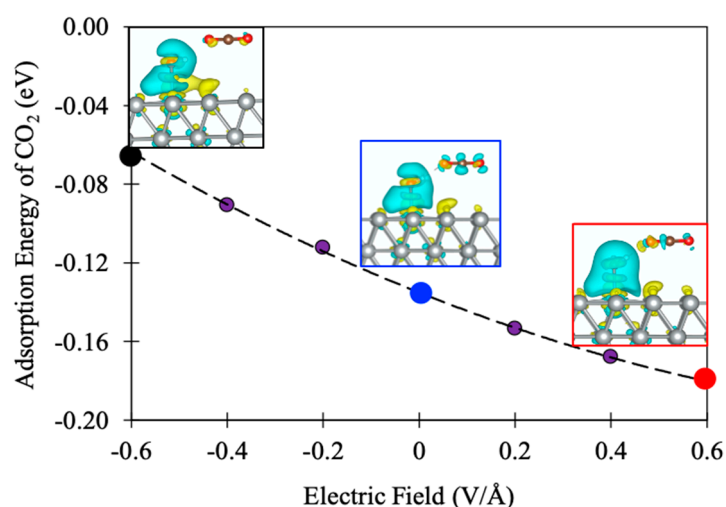


Figure 2. Illustration how an external electric field affects the adsorption strength of CO₂ when water is co-adsorbed on a Ni (111) surface. Red, brown, white, and grey spheres and O, C, H, and Ni atoms, respectively. The yellow or blue areas represent a gain or a loss of electrons at an isosurface of 0.001 electrons/Bohr³.

The first step in overcoming the energetic costs of CO₂ reduction on heterogeneous catalysts is the activation of CO₂. In this study, we investigated the effect of applying an electric-field over YSZ (111) on CO₂ adsorption using density functional theory (DFT)-based calculations. Ultimately, by understanding how both the thermodynamics and kinetics of CO₂ reduction chemistry are influenced by the surface electric field and combining this knowledge with existing knowledge on the applied field effect over CH₄ steam reforming chemistry, we can develop an economically feasible surface electric-field-assisted raw biogas reforming technology that could operate at a lower temperature and S/C ratio than the conventional raw biogas reforming technology.

2. Results and Discussion

2.1. Field-Assisted Oxygen Vacancy Formation on YSZ (111)

An electric field induces charge polarization within the system, which in turn affects the chemical properties of the surface. On the clean YSZ (111) surface, a negative electric field induces charge accumulation toward the surface, while the opposite effect occurs when a positive electric field is applied. We probed the surface reducibility through a water formation reaction, as detailed in the Methods section. The presence of an external electric field was found to decrease the vacancy formation energy values, as compared to when the electric field was absent, by 0.3 and 0.5 eV when we applied a field value of -1 V/\AA and $+1 \text{ V/\AA}$, respectively. This indicates that regardless of the field direction, its presence destabilizes the surface ions. Interestingly, the most favorable oxygen vacancy forms in the $\text{O}_{\text{terminal}}$ site in the absence of field and in the presence of a -1 V/\AA field value, but forms on the $\text{O}_{\text{sublattice}}$ site for the $+1 \text{ V/\AA}$ field case, as shown in Figure 3.

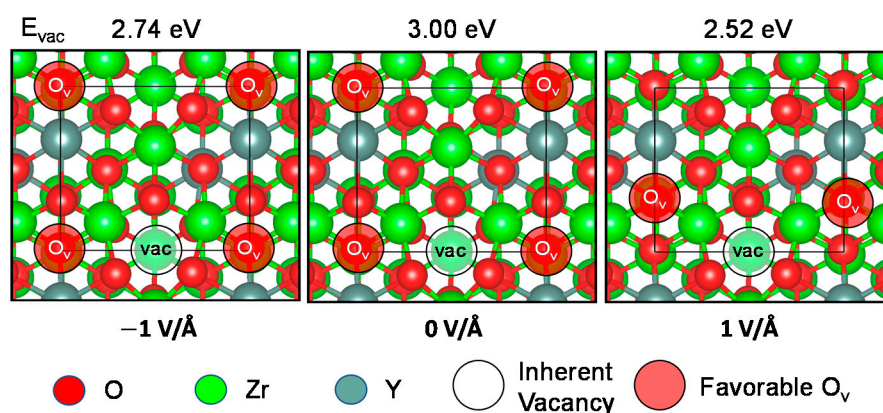


Figure 3. Illustration of the most favorable oxygen vacancy sites (O_v) when a field value of -1 , 0 , and $+1 \text{ V/\AA}$ is applied. Under the -1 and 0 V/\AA field values, O_v occurs on a terminal-O. Under a $+1 \text{ V/\AA}$ field value, O_v occurs on a sublattice-O (2nd atomic layer).

To aid our understanding on the effects of field direction toward the reducibility of YSZ (111), we investigated electronic structure analysis through a partial density of states (PDOS) analysis of the underlying 2 oxygen anions ($\text{O}_{\text{terminal}}$ and $\text{O}_{\text{sublattice}}$) and the Y-cation that lies in between these two anions, as shown in Figure 4. The PDOS of the Y-cation d -state produces a shallow broad peak between -5 eV and the Fermi level (Figure 4a) with similar fillings of 0.94, 0.98, and 1.22 for the 0 V/\AA , $+1 \text{ V/\AA}$, and -1 V/\AA cases, respectively (Table 1). Our Bader charge analysis shown in Table 2 corroborates this calculation, as the partial charge of the Y-cation remains the same for all three cases at ~ 2.20 electrons, indicating that the oxidation state of the cation is unchanged in the presence of an external field. As compared to when the electric field is absent, an applied field of $+1 \text{ V/\AA}$ smears the bonding d -states (Figure 4a.2), while a negative field value of -1 V/\AA shifts both the bonding and the antibonding d -states to slightly lower energy values (Figure 4a.3). We additionally see an increase of antibonding states for the -1 V/\AA case, where the U/N_d ratio increases from 0.74 to 0.76 as compared to when the field is absent (see Table 1). We thus hypothesize that the presence of the electric field causes intra-atomic transitions within the Y-cation d -states, which is a common finding for partially filled d -bands [27].

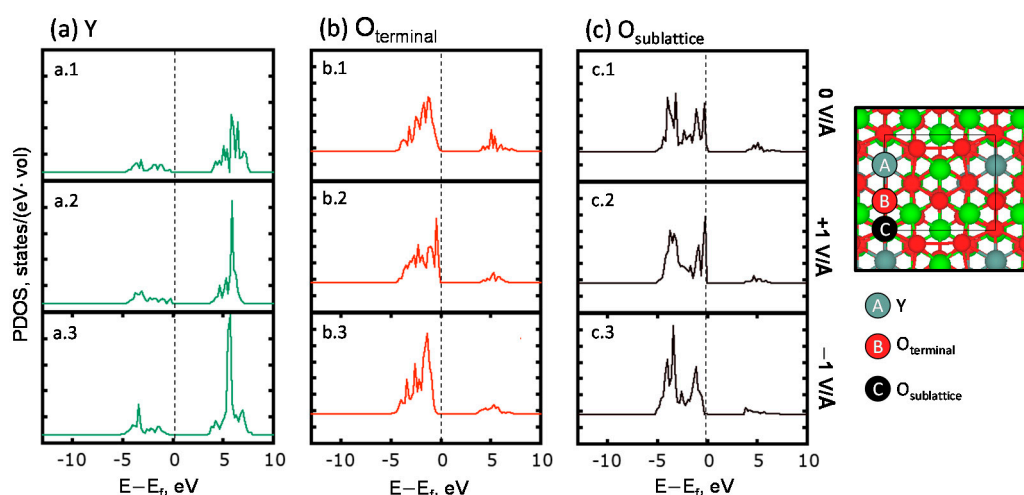


Figure 4. Partial density of states (PDOS) of (a) Y-cation, (b) O_{terminal} and, (c) $O_{\text{sublattice}}$ labeled as A, B and C respectively on the schematic shown on the right, at three different field values of 0, +1, and -1 V/\AA .

Table 1. Quantification of the bonding (below the Fermi energy) and antibonding (above the Fermi energy) PDOS d-states of a Y-cation for applied electric field values of 0, +1, and -1 V/\AA .

Applied Electric Field, V/\AA	Bonding d-States (F), Electrons/vol	Antibonding d-States (U), Electrons/vol	U/(Nd) Ratio
0	0.94	2.73	0.74
1	0.98	2.45	0.71
-1	1.22	3.81	0.76

Table 2. Partial charge assignments of the Y-cation, the O_{terminal} , and the $O_{\text{sublattice}}$ sites as calculated using the Bader charge approach for the three electric field cases: 0, +1, and -1 V/\AA .

Electric Field, V/\AA	Bader Partial Charge = Valence – Bader Charge		
	Y	O_{terminal}	$O_{\text{sublattice}}$
0	2.19	-1.29	-1.33
1	2.20	-1.30	-1.33
-1	2.20	-1.28	-1.33

Figure 4b,c display the PDOS of the p -states of O_{terminal} and $O_{\text{sublattice}}$, where the bonding states correlate with the peaks between -5 and 0 eV . A lowering of the U/N_p ratios in Table 3 indicate that the $+1 \text{ V/\AA}$ and -1 V/\AA field values induce a higher occupancy of the bonding states. We hypothesize that one of the ways the $+1 \text{ V/\AA}$ field value enhances the surface reducibility is by rearranging the p -states to higher energies. The highest-energy state at -0.5 eV intensifies when a field value of $+1 \text{ V/\AA}$ is applied, resulting in weaker bounded states and a lower gap between the occupied and the non-occupied states (Figure 4b.2). We qualitatively could see the same effects with regard to O_{terminal} when a field value of $+1 \text{ V/\AA}$ is applied. We hypothesize that the $O_{\text{sublattice}}$ site is more easily reducible than O_{terminal} under the $+1 \text{ V/\AA}$ field due to a charge accumulation at the $O_{\text{sublattice}}$ site (5.24 vs. 3.28 electrons/vol in Table 3), destabilizing the O-anion. When a field value of -1 V/\AA is applied, we can see a general shift of the O-anion p -states to lower energies, similar to the Y-cation d -states (Figure 4b.3,c.3). While O_{terminal} remains the most reducible O-anion when a field value of -1 V/\AA is applied, its higher-intensity peak at -2 eV shown in Figure 4b.2 weakens the binding of the O-anion with respect to the case when the field is absent.

Table 3. Analysis of PDOS d -states at the O_{terminal} and the $O_{\text{sublattice}}$ sites for applied field values of 0, +1, and -1 V/\AA .

Applied Electric Field, V/\AA	O_{terminal}		$O_{\text{sublattice}}$	
	U/N_p Ratio (p -States)	Total Bonding States ($s + p$), Electrons/vol	U/N_p Ratio (p -States)	Total Bonding States ($s + p$), Electrons/vol
0	0.14	4.36	0.08	4.74
1	0.10	3.28	0.06	5.24
-1	0.11	4.50	0.06	5.31

In summary, the presence of an external electric field results in a rearrangement of the bonding states and affects the total number of available states at the ionic sites as well. As a result, the reducibility of YSZ (111) increases in the presence of an electric field, where a positive field value destabilizes the surface O-anions most strongly.

2.2. Elucidating the Influence of an Electric Field toward CO_2 Activation on YSZ (111)

We tested 10 distinct sites for the adsorption of CO_2 as detailed in the Methods section. Generally, CO_2 bonded more strongly in a Y-cation site, as seen in the Supplementary Materials Figures S1–S3. The adsorption energies of CO_2 in the absence of an electric field were weak, the strongest being -0.21 eV at Site B2 as depicted in the Supplementary Materials Figure S1. The most favorable adsorption configuration is presented again in Figure 5, where the binding is correlated with a differential charge visualization. All evidence points that in the absence of an electric field, no direct charge transfer occurs between CO_2 and the Y-cation. As seen by the charge distribution of the CO_2 molecule and the 3 \AA bond length to the YSZ (111) surface, the bonding predominantly comes from a weak dipole–dipole interaction with CO_2 . The larger ionic radius of the Y-dopant is hypothesized to induce strain and weaken electronic binding within the surface, making the vicinity of the dopant more strongly bonded to the CO_2 reactant.

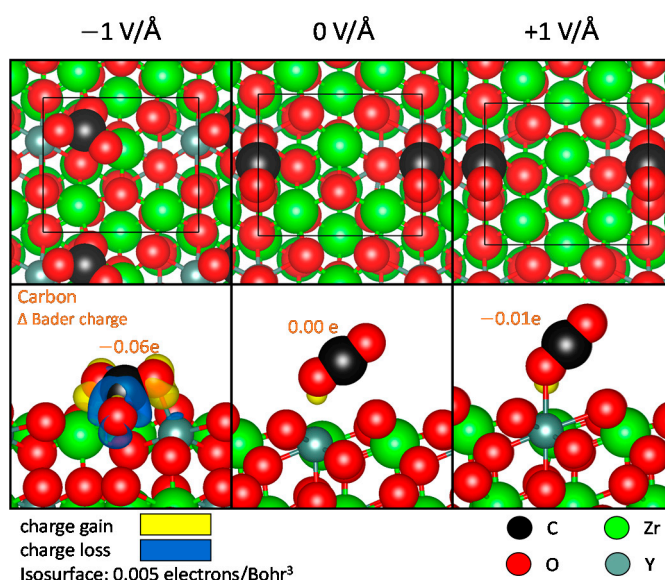


Figure 5. Top and side views of CO_2 adsorption on YSZ (111) under electric fields of -1 , 0 , and $+1 \text{ V/\AA}$. Annotated in orange is the Bader charge difference of carbon (on CO_2) with respect to carbon (on CO_2) when the field is absent.

The orientation of the electric field evidently plays a crucial role toward the capability of the YSZ (111) surface to activate CO_2 . We find that the binding configuration of CO_2 drastically changes when an external electric field of -1 V/\AA is applied, where its well-known linear shape changes to a trigonal planar configuration with a bending angle of $\sim 128^\circ$ (Figure 5). Here, CO_2 bonds to a lattice O, which acts as a Lewis base center

as charge accumulates on the surface ions [17]. The configuration alone indicates that the CO_3^- orbitals are sp^2 hybridized. As a result, the binding of CO_2 is significantly strengthened from -0.21 eV (in the absence of a field) to -0.93 eV at Site T3 as shown in the Supplementary Materials Figure S2. The chemisorption of CO_2 is in turn accompanied by a lengthening of the C–O bond length by 0.1 Å. This also results in a Bader charge change of -0.06 electrons (Figure 5) with respect to when the field was absent and demonstrates that a field value of -1 V/Å transfers charge from the surface to the adsorbed CO_2 molecule, in agreement with the characteristics of an activated CO_2 molecule [16,21]. These results present the potential of harnessing electric fields to tune the thermodynamic conditions for CO_2 activation.

When a $+1$ V/Å field was applied, the bonding between CO_2 and YSZ (111) remains limited due to the dipole–dipole interaction, as shown in Figure 5. Our calculations show, however, that the effect of a positive field value is non-negligible, since it enhances the adsorption strength of CO_2 to -0.43 eV at the same adsorption site (Site B2 in Supplementary Materials Figure S3). All adsorption configurations in the presence of an external field are displayed in Supplementary Materials Figures S2 and S3. We can see that the interaction between the molecule and the surface remained negligible within the vicinity of the Zr cation sites.

A density of states analysis of the adsorption of CO_2 on YSZ (111) is shown in Figure 6a. In the absence of an electric field, the bonding and the antibonding states are present as the -3.6 and 4.8 eV peaks, respectively (Figure 6a.1). When an electric field of $+1$ V/Å is applied, the peaks shift to higher energies, along with a decrease in the total number of states, illustrated by the shallow peaks in Figure 6a.2. We hypothesize that applying a field of $+1$ V/Å pulls electrons away from the CO_2 molecule, resulting in the destabilization of the CO_2 molecular orbitals to higher energies. The weakened binding of electrons within CO_2 thus allows for the stronger interaction with YSZ (111). The partial density of states of the Y- d states in Figure 6b display negligible changes upon the application of a $+1$ V/Å field strength. This further supports that the stronger adsorption induced by the $+1$ V/Å field indeed mainly stems from the response of CO_2 when a field is applied.

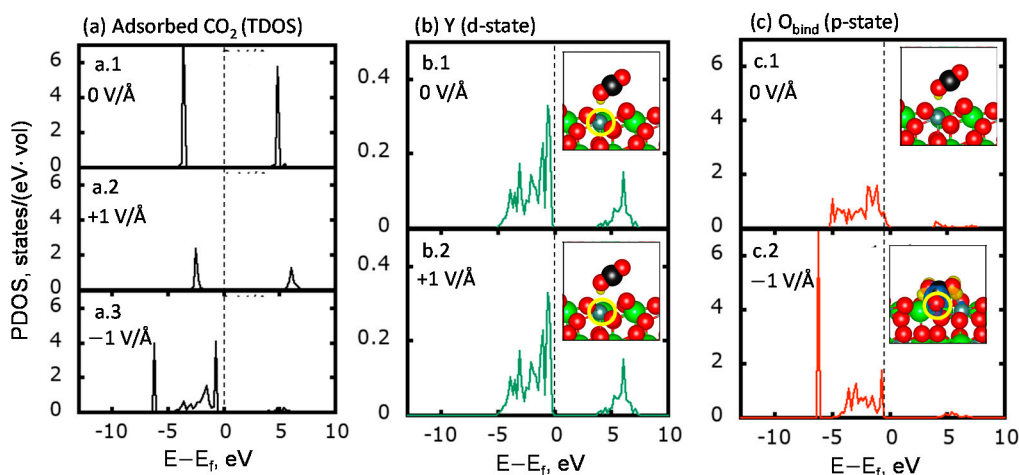


Figure 6. Electronic structure analysis regarding the adsorption of CO_2 on YSZ (111) in the presence and in the absence of an electric field. Density of states analyses comprised of (a) total density of states of an adsorbed CO_2 , (b) d -state PDOS of Y-cation circled in yellow on the subset, and (c) p -state PDOS of O_{bind} circled in yellow on the subset. The black, red, dark-green, and light-green spheres are C, O, Y, and Zr, respectively.

On the other hand, when a negative electric field is applied, strong chemisorption of CO_2 occurs, which is also consequently reflected in its total density of states. As shown in Figure 6a.3, the bonding of CO_2 to the lattice O results in a lowering of the bonding states in the presence of a negative electric field. In addition, the antibonding states are now below the Fermi energy. Charge transfer occurs from the lattice O, which was also

evident by the increased total number of bonding states within CO_2 , from 3.76 electrons to 9.22 electrons/vol, with respect to when the field is absent. We also observe a smearing of the CO_2 states within the -5 and 0 eV range, which implies that the electronic state energy levels were now more closely spaced.

The partial density of states of the p -states within the CO_2 -bounded lattice O highlighted in yellow (O_{bind}) is given in Figure 6c. We can see that the electronic states of O_{bind} lie between -5 and 0 eV in the absence of a field (Figure 6c.1). Upon the chemisorption of CO_2 when a -1 V/Å field was applied, a splitting of the p -orbitals occurs, as revealed by the emergence of a new peak at -6.24 eV (Figure 6c.2). Ultimately, the chemisorption between O_{bind} and the CO_2 molecule is reflected through changes within their density of states.

3. Computational Methods

Electronic structure calculations were done under the density functional theory framework using the Vienna *Ab initio* Software Package (VASP) [28,29]. We used a planewave basis, through the Projector Augmented Wave (PAW) approach, using the PAW potentials that were released in 2015 [30], to expand the one-electron orbital wavefunctions for the electron density [31]. The kinetic cutoff energy for the planewave basis was 500 eV. The exchange-correlation function employed was the Perdew, Burke, and Ernzerhof (PBE) model within the generalized gradient approximation (GGA) level of theory [32]. Spin-polarized calculations were conducted to provide degrees of freedom for the electron filling. The Gaussian smearing method was used to treat the Fermi level with a width of 0.1 eV. The optimization criterion for the self-consistent field (SCF) cycle and ionic relaxation were 10^{-6} eV and 10^{-2} eV/Å, respectively. As previously reported, the optimized bulk lattice constant of ZrO_2 was 5.12 Å [33].

To examine the effects of the external electric field toward CO_2 adsorption, we used a 35-atom (1×1) YSZ (111) surface consisting of 3 stoichiometric layers, based on the unit cell proposed by Shishkin and Ziegler displayed in Figure 7 [34]. In this calculational setup, the bottom two stoichiometric layers were fixed at their bulk positions, while the first top layer was allowed to relax. The elementary building unit of YSZ closely resembles 9 mol% concentration of Ytria, where an oxygen vacancy compensates the charge imbalance induced from substituting a single formula unit of Y_2O_3 into a cubic ZrO_2 lattice [34]. A Monkhorst-Pack [35] mesh with a grid of $(4 \times 4 \times 1)$ k -points was chosen for the Brillouin zone integration for the 7.24×6.27 Å unit cell. The level of the theory of the model was justified from previous studies, as the choice between PBE and DFT + U did not change trends induced by external electric fields [33,36].

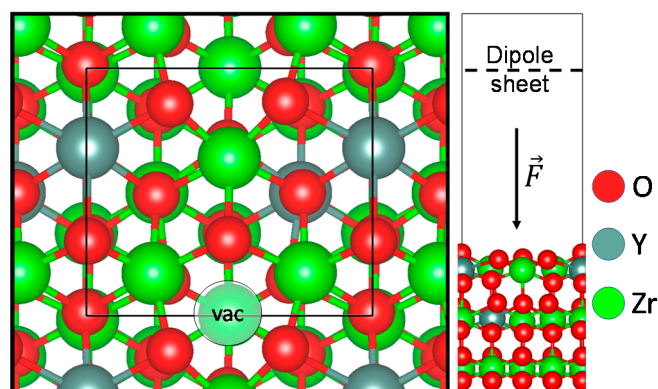


Figure 7. Schematic of the (1×1) YSZ (111) model used in the study. The inherent vacancy site annotated on the top view is created upon charge balancing the doping of Y_2O_3 into ZrO_2 . Annotated by the black arrow on the side view is the direction of a negative field.

A uniform electric field was applied in our DFT-based model using the approach proposed by Neugebauer and Scheffler [37]. The method consists of modeling an artificial dipole sheet in the vacuum center. A 15 Å vacuum was introduced to the unit cell to avoid “charge sloshing” from the interaction between periodic unit cells [38]. We considered three electric field scenarios in our system: -1.0 , 0.0 , and $+1.0$ V/Å. The direction of the negative electric field was defined to point perpendicularly toward the surface, causing charge to be accumulated on the surface, as annotated in Figure 7. The reverse convention is true for the positive electric field.

Charge polarization within the slab induced by an external electric field is bound to change the chemical properties of the surface. The effect of an external electric field on YSZ (111) was applied perpendicularly to its surface, $\vec{F} = F\hat{z}$. The surface reducibility was probed using the water formation reaction, with the reaction energy defined in Equation (1):

$$E_{\text{vac}}(\vec{F}) = E_{\text{YSZ}(111)+\text{vac}}(\vec{F}) + E_{\text{H}_2\text{O}(\text{g})}(\vec{F}) - E_{\text{YSZ}(111)}(\vec{F}) - E_{\text{H}_2(\text{g})}(\vec{F}) \quad (1)$$

where $E_{\text{YSZ}(111)+\text{vac}}(\vec{F})$ and $E_{\text{YSZ}}(\vec{F})$ are the field-dependent total energies of the clean YSZ (111) slab with and without an additional oxygen vacancy, respectively, and $E_{\text{H}_2\text{O}(\text{g})}(\vec{F})$ and $E_{\text{H}_2(\text{g})}(\vec{F})$ are total energies of isolated gas-phase water and hydrogen molecules, respectively, with an orientation that is perpendicular to the externally applied electric field. A negative vacancy formation energy means that the reaction is exothermic, and a positive value indicates the reverse.

To investigate effects of the electric field toward the adsorption of CO_2 on YSZ (111), we compared their adsorption energies as defined in Equation (2):

$$E_{\text{ads}}(\vec{F}) = E_{\text{CO}_2/\text{YSZ}(111)}(\vec{F}) - (E_{\text{CO}_2(\text{g})}(\vec{F}) + E_{\text{YSZ}(111)}(\vec{F})) \quad (2)$$

where $E_{\text{CO}_2/\text{YSZ}(111)}(\vec{F})$ and $E_{\text{YSZ}(111)}(\vec{F})$ are field-dependent total energies of the CO_2 -adsorbed and clean YSZ (111) surfaces, respectively. $E_{\text{CO}_2(\text{g})}(\vec{F})$ is the field-dependent total energy of CO_2 in the gas phase. A negative value of $E_{\text{ads}}(\vec{F})$ indicates stronger binding of the molecule with the surface, while a positive value points to a repulsive interaction. The adsorption sites tested in this study are labeled in Figure 8, consisting of the various top (T), bridge (B), and hollow (H) sites.

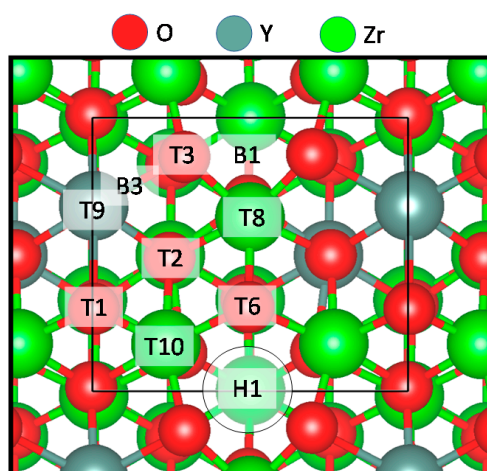


Figure 8. Initial CO_2 adsorption sites that were tested on the (1×1) YSZ (111) cell.

Charge exchange upon the adsorption of CO₂ on YSZ (111) was visualized in VESTA by calculating the frozen charge density difference at the optimized bonding geometry, described in Equation (3). In this paper, we refer to this as the differential charge analysis.

$$\Delta n(\vec{F}, \vec{r}) = n_{\text{CO}_2/\text{YSZ}(111)}(\vec{F}, \vec{r}) - (n_{\text{CO}_2(\text{g})}(\vec{F}, \vec{r}) + n_{\text{YSZ}(111)}(\vec{F}, \vec{r})) \quad (3)$$

where n_x is the notation for charge distribution of an optimized structure indicated by the subscripts. Within the visualization, a negative charge accumulation is displayed by a yellow electron density cloud, and charge loss is signified in blue. Quantification of the partial charge transfer is then conducted through a Bader charge analysis employing the algorithm proposed by Henkelman et al. [39]. A negative Bader charge is associated with negatively charged ions. It must be noted that while Bader charge correlates directly to oxidation number, it has also been established that the Bader charge alone cannot determine the exact oxidation state of the ion [40].

We also investigated the changes within the surface electronic structures through the analysis of their density of states. The ratio of antibonding/total states and total number of electronic states can be calculated using Equations (4) and (5), respectively, where the latter is simply an integration under the curve [41]:

$$U/N = \frac{\int_{E_{\text{Fermi}}}^{+\infty} \rho(E) dE}{\int_{-\infty}^{+\infty} \rho(E) dE} \quad (4)$$

$$N = \int_{-\infty}^{+\infty} \rho(E) dE \quad (5)$$

where E is the energy level, $\rho(E)$ is the density of electronic states at a given energy, and E_{Fermi} is the Fermi energy.

Finally, the computational setup for the calculations shown in Figure 2 on Ni (111) was previously reported in our previous work [42]. These calculations were performed in a p (3×3) supercell. A Monkhorst-Pack [35] mesh with a grid of ($4 \times 4 \times 1$) k -points was chosen for the Brillouin zone integration. The adsorption energy as plotted is defined as

$$E_{\text{ads}}(\vec{F}) = E_{(\text{CO}_2+\text{H}_2\text{O})/\text{Ni}(111)}(\vec{F}) - E_{\text{H}_2\text{O}/\text{Ni}(111)}(\vec{F}) - E_{\text{CO}_2}(\vec{F}) \quad (6)$$

where $E_{(\text{CO}_2+\text{H}_2\text{O})/\text{Ni}(111)}(\vec{F})$ is the field-dependent total energy of the CO₂ and H₂O co-adsorbed surface on Ni (111), $E_{\text{H}_2\text{O}/\text{Ni}(111)}(\vec{F})$ is the field-dependent total energy of the water-covered Ni (111) surface, and $E_{\text{CO}_2}(\vec{F})$ is the field-dependent total energy of a CO₂ molecule in the gas phase.

4. Conclusions

To harness electric fields for enhancing CO₂ reduction, we first need an understanding of its effects toward CO₂ activation. As CO₂ is inherently inert, chemisorbing CO₂ is typically one of the most energetically costly processes for heterogeneous catalysts [17]. We conducted a DFT study focusing on the electronic interactions between CO₂ and YSZ (111) under the influence of a positive (+1 V/Å) and a negative electric field (−1 V/Å) and compared our results to when the field is absent.

By comparing the oxygen formation energies within these three cases, we found that an electric field destabilizes surface O-ions on YSZ (111), where a +1 V/Å field value increases the reducibility of the surface by the largest extent. Destabilization was further reflected in a surface ion PDOS analysis by either increasing the density of higher-energy bonding states or by shifting bonding states closer to the Fermi energy. We also found that by inverting the direction of the electric field vector toward the surface (i.e., applying a −1 V/Å field value), the most favorable oxygen vacancy site changes from the O anion in

the first layer (O_{terminal}) to O in the second atomic layer ($O_{\text{sublattice}}$). Ultimately, our studies show that an external electric field influences the surface states of YSZ (111).

Upon the adsorption of CO_2 on YSZ (111), we generally found that it binds more favorably within the vicinity of the Y-cation. Without the presence of an electric field, CO_2 binds with the surface through a weak dipole–dipole interaction. When a $-1 \text{ V}/\text{\AA}$ field value is applied, CO_2 becomes chemisorbed to the surface and forms a CO_3^- complex with the surface O. The strong interaction is reflected upon the direct charge transfer to the adsorbate (through the gain of 0.06 electrons) and the orbital splitting observed within the O_{lattice} p -states. While CO_2 remains physisorbed when a $+1 \text{ V}/\text{\AA}$ field value is applied, our total density of states analysis indicates that a positive field pulls charge away from the adsorbate resulting in a shift of its bonding and antibonding peaks to higher energies, allowing a stronger interaction with YSZ (111). This explains why the adsorption energy of CO_2 was relatively stronger by 0.2 eV. Ultimately, the effect of an electric field toward CO_2 adsorption is not negligible, and there is potential in utilizing electric fields to favor the thermodynamics of CO_2 reduction.

Supplementary Materials: The following are available online at <https://www.mdpi.com/2073-4344/11/2/271/s1>; Figure S1: Comparison of CO_2 adsorption sites and their corresponding adsorption energies on YSZ (111) in the absence of an electric field. Highlighted in pink is the most favorable adsorption site; Figure S2: Comparison of CO_2 adsorption sites and their corresponding adsorption energies on YSZ (111) when a $-1 \text{ V}/\text{\AA}$ external electric field is applied. Highlighted in pink is the most favorable adsorption site. The legend for each species is shown in Figure S1; Figure S3: Comparison between the CO_2 adsorption sites and their corresponding adsorption energies on YSZ (111) when a $+1 \text{ V}/\text{\AA}$ external electric field is applied. Highlighted in pink is the most favorable adsorption site. The legend for each species is shown in Figure S1.

Author Contributions: Conceptualization, N.U., F.C., J.-I.Y., S.H., and J.-S.M.; methodology, N.U. and J.-S.M.; software, N.U.; validation, N.U., F.C., S.H., and J.-S.M.; formal analysis, N.U.; investigation, N.U., F.C., J.-I.Y., S.H., and J.-S.M.; resources, J.-I.Y., S.H., and J.-S.M.; data curation, N.U.; writing—original draft preparation, N.U., S.H., and J.-S.M.; writing—review and editing, N.U., F.C., S.H., and J.-S.M.; visualization, N.U.; supervision, J.-S.M.; project administration, S.H. and J.-S.M.; funding acquisition, J.-I.Y., S.H., and J.-S.M. All authors have read and agreed to the published version of the manuscript.

Funding: Funding by the Research and Development Program of the Korea Institute of Energy Research (KIER) (No. C1-2438) is gratefully acknowledged. This work was partially funded by the Joint Center for Deployment and Research in Earth Abundant Materials (JCDREAM) in Washington State.

Institutional Review Board Statement: Not applicable.

Informed Consent Statement: Not applicable.

Data Availability Statement: The data presented in this study are available upon request from the corresponding author.

Acknowledgments: Part of the computational resources was also provided by the Kamiak HPC under the Center for Institutional Research Computing at Washington State University. The Pacific Northwest National Laboratory is operated by Battelle for the U.S. DOE.

Conflicts of Interest: The authors declare no conflict of interest.

References

1. Pham Minh, D.; Siang, T.J.; Vo, D.-V.N.; Phan, T.S.; Ridart, C.; Nzihou, A.; Grouset, D. *Chapter 4—Hydrogen Production from Biogas Reforming: An Overview of Steam Reforming, Dry Reforming, Dual Reforming, and Tri-Reforming of Methane*; Azzaro-Pantel, C., Ed.; Academic Press, Elsevier: New York, NY, USA, 2018; pp. 111–166. ISBN 978-0-12-811197-0. [CrossRef]
2. Nalbant, Y.; Colpan, C.O. *An Overview of Hydrogen Production from Biogas BT—Accelerating the Transition to a 100% Renewable Energy Era*; Uyar, T.S., Ed.; Springer International Publishing: Cham, Switzerland, 2020; pp. 355–373. ISBN 978-3-030-40738-4.
3. Nehring, R. Traversing the mountaintop: World fossil fuel production to 2050. *Philos. Trans. R. Soc. B Biol. Sci.* **2009**, *364*, 3067–3079. [CrossRef] [PubMed]

4. Lelieveld, J.; Klingmüller, K.; Pozzer, A.; Burnett, R.T.; Haines, A.; Ramanathan, V. Effects of fossil fuel and total anthropogenic emission removal on public health and climate. *Proc. Natl. Acad. Sci. USA* **2019**, *116*, 7192. [[CrossRef](#)] [[PubMed](#)]
5. Hoel, M.; Kverndokk, S. Depletion of fossil fuels and the impacts of global warming. *Resour. Energy Econ.* **1996**, *18*, 115–136. [[CrossRef](#)]
6. Pareek, A.; Dom, R.; Gupta, J.; Chandran, J.; Adepu, V.; Borse, P.H. Insights into renewable hydrogen energy: Recent advances and prospects. *Mater. Sci. Energy Technol.* **2020**, *3*, 319–327. [[CrossRef](#)]
7. Staffell, I.; Scamman, D.; Velazquez Abad, A.; Balcombe, P.; Dodds, P.E.; Ekins, P.; Shah, N.; Ward, K.R. The role of hydrogen and fuel cells in the global energy system. *Energy Environ. Sci.* **2019**, *12*, 463–491. [[CrossRef](#)]
8. Marcoberardino, G.; Vitali, D.; Spinelli, F.; Binotti, M.; Manzolini, G. Green Hydrogen Production from Raw Biogas: A Techno-Economic Investigation of Conventional Processes Using Pressure Swing Adsorption Unit. *Processes* **2018**, *6*, 19. [[CrossRef](#)]
9. Alves, H.J.; Bley Junior, C.; Niklevicz, R.R.; Frigo, E.P.; Frigo, M.S.; Coimbra-Araújo, C.H. Overview of hydrogen production technologies from biogas and the applications in fuel cells. *Int. J. Hydrogen Energy* **2013**, *38*, 5215–5225. [[CrossRef](#)]
10. Gray, J.T.; Che, F.; McEwen, J.-S.; Ha, S. Field-assisted suppression of coke in the methane steam reforming reaction. *Appl. Catal. B Environ.* **2020**, *260*, 118132. [[CrossRef](#)]
11. Che, F.; Gray, J.T.; Ha, S.; Kruse, N.; Scott, S.L.; McEwen, J.-S. Elucidating the Roles of Electric Fields in Catalysis: A Perspective. *ACS Catal.* **2018**, *8*, 5153–5174. [[CrossRef](#)]
12. Che, F.; Gray, J.T.; Ha, S.; McEwen, J.-S. Improving Ni Catalysts Using Electric Fields: A DFT and Experimental Study of the Methane Steam Reforming Reaction. *ACS Catal.* **2017**, *7*, 551–562. [[CrossRef](#)]
13. Che, F.; Gray, J.T.; Ha, S.; McEwen, J.-S. Catalytic water dehydrogenation and formation on nickel: Dual path mechanism in high electric fields. *J. Catal.* **2015**, *332*, 187–200. [[CrossRef](#)]
14. Kim, S.S.; Lee, H.H.; Hong, S.C. A study on the effect of support's reducibility on the reverse water-gas shift reaction over Pt catalysts. *Appl. Catal. A Gen.* **2012**, *423–424*, 100–107. [[CrossRef](#)]
15. Bernal, S.; Blanco, G.; Gatica, J.M.; Larese, C.; Vidal, H. Effect of Mild Re-oxidation Treatments with CO₂ on the Chemisorption Capability of a Pt/CeO₂ Catalyst Reduced at 500 °C. *J. Catal.* **2001**, *200*, 411–415. [[CrossRef](#)]
16. Zhu, M.; Ge, Q.; Zhu, X. Catalytic Reduction of CO₂ to CO via Reverse Water Gas Shift Reaction: Recent Advances in the Design of Active and Selective Supported Metal Catalysts. *Trans. Tianjin Univ.* **2020**, *26*, 172–187. [[CrossRef](#)]
17. Wang, L.; Chen, W.; Zhang, D.; Du, Y.; Amal, R.; Qiao, S.; Wu, J.; Yin, Z. Surface strategies for catalytic CO₂ reduction: From two-dimensional materials to nanoclusters to single atoms. *Chem. Soc. Rev.* **2019**, *48*, 5310–5349. [[CrossRef](#)] [[PubMed](#)]
18. Köck, E.M.; Kogler, M.; Bielz, T.; Klötzer, B.; Penner, S. In situ FT-IR spectroscopic study of CO₂ and CO adsorption on Y₂O₃, ZrO₂, and yttria-stabilized ZrO₂. *J. Phys. Chem. C* **2013**, *117*, 17666–17673. [[CrossRef](#)] [[PubMed](#)]
19. Goguet, A.; Meunier, F.C.; Tibiletti, D.; Breen, J.P.; Burch, R. Spectrokinetic investigation of reverse water-gas-shift reaction intermediates over a Pt/CeO₂ catalyst. *J. Phys. Chem. B* **2004**, *108*, 20240–20246. [[CrossRef](#)]
20. Bobadilla, L.F.; Santos, J.L.; Ivanova, S.; Odriozola, J.A.; Urakawa, A. Unravelling the Role of Oxygen Vacancies in the Mechanism of the Reverse Water–Gas Shift Reaction by Operando DRIFTS and Ultraviolet–Visible Spectroscopy. *ACS Catal.* **2018**, *8*, 7455–7467. [[CrossRef](#)]
21. Álvarez, A.; Borges, M.; Corral-Pérez, J.J.; Olcina, J.G.; Hu, L.; Cornu, D.; Huang, R.; Stoian, D.; Urakawa, A. CO₂ Activation over Catalytic Surfaces. *ChemPhysChem* **2017**, *18*, 3135–3141. [[CrossRef](#)]
22. Xiao, H.; Goddard, W.A.; Cheng, T.; Liu, Y. Cu metal embedded in oxidized matrix catalyst to promote CO₂ activation and CO dimerization for electrochemical reduction of CO₂. *Proc. Natl. Acad. Sci. USA* **2017**, *114*, 6685–6688. [[CrossRef](#)] [[PubMed](#)]
23. Daza, Y.A.; Kuhn, J.N. CO₂ conversion by reverse water gas shift catalysis: Comparison of catalysts, mechanisms and their consequences for CO₂ conversion to liquid fuels. *RSC Adv.* **2016**, *6*, 49675–49691. [[CrossRef](#)]
24. Oshima, K.; Shinagawa, T.; Nogami, Y.; Manabe, R.; Ogo, S.; Sekine, Y. Low temperature catalytic reverse water gas shift reaction assisted by an electric field. *Catal. Today* **2014**, *232*, 27–32. [[CrossRef](#)]
25. Lamberts, S.V.; Barroo, C.; Owczarek, S.; Jacobs, L.; Genty, E.; Gilis, N.; Kruse, N.; Visart de Bocarmé, T. Adsorption and Hydrogenation of CO₂ on Rh Nanosized Crystals: Demonstration of the Role of Interfacet Oxygen Spillover and Comparative Studies with O₂, N₂O, and CO. *J. Phys. Chem. C* **2017**, *121*, 16238–16249. [[CrossRef](#)]
26. Calvaresi, M.; Martinez, R.V.; Losilla, N.S.; Martinez, J.; Garcia, R.; Zerbetto, F. Splitting CO₂ with Electric Fields: A Computational Investigation. *J. Phys. Chem. Lett.* **2010**, *1*, 3256–3260. [[CrossRef](#)]
27. Sterrer, M.; Freund, H.-J. Properties of Oxide Surfaces. *Surf. Interface Sci.* **2013**, 229–278. [[CrossRef](#)]
28. Kresse, G.; Furthmüller, J. Efficient iterative schemes for ab initio total-energy calculations using a plane-wave basis set. *Phys. Rev. B Condens. Matter Mater. Phys.* **1996**, *54*, 11169–11186. [[CrossRef](#)] [[PubMed](#)]
29. Kresse, G.; Hafner, J. Ab initio molecular dynamics for liquid metals. *Phys. Rev. B* **1993**, *47*, 558. [[CrossRef](#)] [[PubMed](#)]
30. Lejaeghere, K.; Bihlmayer, G.; Björkman, T.; Blaha, P.; Blügel, S.; Blum, V.; Caliste, D.; Castellì, I.E.; Clark, S.J.; Dal Corso, A.; et al. Reproducibility in density functional theory calculations of solids. *Science* **2016**, *351*, aad3000. [[CrossRef](#)] [[PubMed](#)]
31. Kresse, G.; Joubert, D. From ultrasoft pseudopotentials to the projector augmented-wave method. *Phys. Rev. B* **1999**, *59*, 11–19. [[CrossRef](#)]
32. Perdew, J.P.; Burke, K.; Ernzerhof, M. Generalized Gradient Approximation Made Simple. *Phys. Rev. Lett.* **1996**, *77*, 3865–3868. [[CrossRef](#)]

33. Che, F.; Ha, S.; McEwen, J.S. Elucidating the role of the electric field at the Ni/YSZ electrode: A DFT study. *J. Phys. Chem. C* **2016**, *120*, 14608–14620. [[CrossRef](#)]
34. Shishkin, M.; Ziegler, T. Oxidation of H₂, CH₄, and CO molecules at the interface between nickel and yttria-stabilized zirconia: A theoretical study based on DFT. *J. Phys. Chem. C* **2009**, *113*, 21667–21678. [[CrossRef](#)]
35. Monkhorst, H.J.; Pack, J.D. Special points for Brillouin-zone integrations. *Phys. Rev. B* **1976**, *13*, 5188–5192. [[CrossRef](#)]
36. Che, F.; Ha, S.; McEwen, J.S. Hydrogen Oxidation and Water Dissociation over an Oxygen-Enriched Ni/YSZ Electrode in the Presence of an Electric Field: A First-Principles-Based Microkinetic Model. *Ind. Eng. Chem. Res.* **2017**, *56*, 1201–1213. [[CrossRef](#)]
37. Neugebauer, J.; Scheffler, M. Adsorbate-substrate and adsorbate-adsorbate interactions of Na and K adlayers on Al(111). *Phys. Rev. B* **1992**, *46*. [[CrossRef](#)] [[PubMed](#)]
38. Feibelman, P.J. Surface-diffusion mechanism versus electric field: Pt/Pt(001). *Phys. Rev. B Condens. Matter Mater. Phys.* **2001**, *64*, 1–6. [[CrossRef](#)]
39. Henkelman, G.; Arnaldsson, A.; Jónsson, H. A fast and robust algorithm for Bader decomposition of charge density. *Comput. Mater. Sci.* **2006**, *36*, 354–360. [[CrossRef](#)]
40. Wiberg, K.B.; Rablen, P.R. Comparison of atomic charges derived via different procedures. *J. Comput. Chem.* **1993**, *14*, 1504–1518. [[CrossRef](#)]
41. Nørskov, J.K.; Studt, F.; Abild-Pedersen, F.; Bligaard, T. *Fundamental Concepts in Heterogeneous Catalysis*; John Wiley & Sons, Inc.: Hoboken, NJ, USA, 2014; ISBN 9781118892114.
42. Che, F.; Zhang, R.; Hensley, A.J.; Ha, S.; McEwen, J.-S. Density functional theory studies of methyl dissociation on a Ni(111) surface in the presence of an external electric field. *Phys. Chem. Chem. Phys.* **2014**, *16*, 2399–2410. [[CrossRef](#)] [[PubMed](#)]